UCSF
UC San Francisco Previously Published Works

Title

[11C]Paraoxon: Radiosynthesis, Biodistribution and In Vivo Positron Emission Tomography Imaging in Rat.

Permalink

https://escholarship.org/uc/item/9sd0k4sn

Journal

Journal of Pharmacology and Experimental Therapeutics, 388(2)

Authors

Hayes, Thomas
Chao, Chih-Kai
Huynh, Tony
et al.

Publication Date

2024-01-17

DOI

10.1124/jpet.123.001832

Copyright Information

Peer reviewed

Special Section on Medical Countermeasures

[11C]Paraoxon: Radiosynthesis, Biodistribution and In Vivo Positron Emission Tomography Imaging in Rat⑤

Thomas R. Hayes, Chih-Kai Chao, Joseph E. Blecha, Tony L. Huynh, Henry F. VanBrocklin, Kurt R. Zinn, John M. Gerdes, and ⑩ Charles M. Thompson

Department of Biomedical and Pharmaceutical Sciences, University of Montana, Missoula, Montana (C.-K.C., J.M.G., C.M.T.); Department of Radiology and Biomedical Imaging, University of California, San Francisco, San Francisco, California (T.R.H., J.E.B., T.L.H., H.F.V.); and Departments of Radiology, Small Animal Clinical Sciences, and Biomedical Engineering and Institute for Quantitative Health Science and Engineering, Michigan State University, East Lansing, Michigan (K.R.Z.)

ABSTRACT

Synthesis of the acetylcholinesterase inhibitor paraoxon (POX) as a carbon-11 positron emission tomography tracer ([11C]POX) and profiling in live rats is reported. Naïve rats intravenously injected with [11C]POX showed a rapid decrease in parent tracer to ∼1%, with an increase in radiolabeled serum proteins to 87% and red blood cells (RBCs) to 9%. Protein and RBC leveled over 60 minutes, reflecting covalent modification of proteins by [11C]POX. Ex vivo biodistribution and imaging profiles in naïve rats had the highest radioactivity levels in lung followed by heart and kidney, and brain and liver the lowest. Brain radioactivity levels were low but observed immediately after injection and persisted over the 60-minute experiment. This showed for the first time that even low POX exposures (∼200 ng tracer) can rapidly enter brain. Rats given an LD_{50} dose of nonradioactive paraoxon at the LD_{50} 20 or 60 minutes prior to [11C]POX tracer revealed that protein pools were blocked. Blood radioactivity at 20 minutes was markedly lower than naïve levels due to rapid protein modification by nonradioactive POX; however, by 60 minutes the blood radioactivity returned to near naïve levels. Live rat tissue imaging-derived radioactivity values were 10%–37% of naïve levels in nonradioactive POX pretreated rats at 20 minutes, but by 60 minutes the area under the curve (AUC) values had recovered to 25%–80% of naïve. The live rat imaging supported blockade by nonradioactive POX pretreatment at 20 minutes and recovery of proteins by 60 minutes.

SIGNIFICANCE STATEMENT

Paraoxon (POX) is an organophosphorus (OP) compound and a powerful prototype and substitute for OP chemical warfare agents (CWAs) such as sarin, VX, etc. To study the distribution and penetration of POX into the central nervous system (CNS) and other tissues, a positron emission tomography (PET) tracer analog, carbon-11–labeled paraoxon ([11C]POX), was prepared. Blood and tissue radioactivity levels in live rats demonstrated immediate penetration into the CNS and persistent radioactivity levels in tissues indicative of covalent target modification.

Introduction

Paraoxon (POX; O,O-diethyl-O-p-nitrophenylphosphate) is the highly reactive metabolite of the organophosphorus (OP)

insecticide parathion (Davison, 1953; Neal, 1967; Lichtenstein et al., 1973) and a potent inhibitor of the acetylcholine neurotransmitter-processing enzyme acetylcholinesterase (AChE). In vitro, POX is only slightly less potent an inhibitor of AChE than chemical warfare agents (CWAs) such as soman, sarin, VX, etc. and is therefore considered highly toxic (Volpe et al., 1990; Kardos and Sultatos, 2000). POX inhibits AChE by covalent phosphorylation of the active site serine (Fig. 1) blocking further catalytic action. The mechanism of AChE phosphorylation proceeds via ejection of the leaving group p-nitrophenol.

In vivo, POX inhibition of AChE occurs in blood, the central nervous system (CNS), and peripheral tissues, increasing

ABBREVIATIONS: AChE, acetylcholinesterase; AUC, area under the curve; bioD, biodistribution; [11C]POX, carbon-11–labeled paraoxon; CNS, central nervous system; CT, computed tomography; CWA, chemical warfare agent; DMF, dimethylformamide; GBq, gigabecquerel; HPLC, high-performance liquid chromatography; ID, injected dose; MR, magnetic resonance; NMR, nuclear magnetic resonance; OP, organophosphate; PET, positron emission tomography; POX, paraoxon; RBC, red blood cell; ROI, region of interest; SUV, standardized uptake value; $t_{1/2}$, half-life; TAC, time-activity curve.
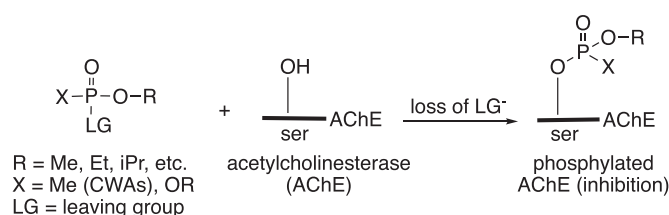
Fig. 1. Phosphorylation of AChE by organophosphorus compounds (paraoxon: LG, OPhNO₂; R, Et; X, OR).

synaptic acetylcholine (ACh) levels and subsequent cholinergic excitotoxicity (Volpe et al., 1990; Blomqvist et al., 2001). Seizures and irreversible neuronal damage can result from sustained AChE inhibition (Zare et al., 2020) and can result in death (Ballantyne and Marrs, 1992; Morita, 1995; Eisenkraft et al., 2013; Farizatto and Bahr, 2017; Taylor, 2018). Asymptomatic, low-level exposures to POX can also render the brain vulnerable (Song et al., 2004) or cause neurologic problems (Farizatto and Bahr, 2017).

Due to its structural, mechanistic, and toxicologic similarities to many CWAs, POX has become the prototype organophosphorus compound for neurotoxicity studies, as the extreme lethality of CWAs limits their practical use in research. POX is nonvolatile, contains a chromophore, is easily hydrolyzed for disposal, and lacks asymmetry that further simplifies its use in toxicologic studies. Thus, POX has become the standard for molecular, cellular, and/or organismal investigations of OP exposure, new and existing antidotes, antiseizure drugs, and neurotoxicity.

Despite common use as a model OP agent, there are few pharmacokinetic (PK), pharmacodynamic (PD), or biodistribution properties (Gearhart et al., 1994) of POX, which is surprising given that rat POX $LD_{50} = 250$ μg/kg. This limits our understanding of how POX enters tissues, especially the CNS, to inactivate its key target, AChE. To address these deficiencies, a positron emission tomography (PET) carbon-11 [half-life $(t_{1/2}) = 20$ minutes]–radiolabeled version of POX ([11C]POX; Fig. 2) was prepared to conduct PK/PD profiles in live rats and to quantify radioactivity presence in tissues (Timchalk et al., 2002; Ametamey et al., 2008). The primary advantage of a carbon-11 isotope PET tracer analog versus H-3 or C-14 analogs is the opportunity to conduct dynamic analyses in live subjects with superior sensitivity. Carbon-11 is a relatively short-lived radioisotope ($t_{1/2} \sim 20$ minutes), with approximately 100–120 minutes (5 to 6 half-lives or 1.5%–3% remaining radioactivity) of useful experimental time [for review, see Goud et al. (2021)]. The brief half-life for carbon-11 required a number of tactical and experimental challenges to be overcome; however, substitution of the 11C-isotope retains the identical pharmacokinetics, pharmacodynamics, and mechanism.

Quantitative PET imaging furnishes the exceptional sensitivity needed to assess ultralow (nanogram to picogram) levels of a highly reactive, toxic compound in vivo such as POX. A POX-based PET tracer offers an excellent probe in live tissues capable
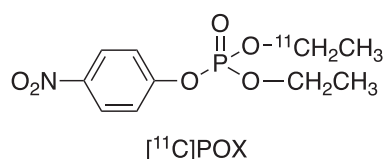
of interrogating in real time quantitative tissue radioactivity distributions of molecular level events—a distinct advantage to mass spectrometry, nuclear magnetic resonance/magnetic resonance imaging (NMR/MRI), or other methodologies.

Of relevance to this work, PET studies have used AChE substrate tracers (Koeppe et al., 1999; Kikuchi et al., 2010), AChE inhibitors (Planas et al., 1994; Pappata et al., 1996; Shinotoh et al., 2004; Hiraoka et al., 2009), and cholinergic receptors agents (Volkow et al., 2001). The development of [11C]POX as an OP PET tracer follows our previous work on the biodistribution of O-(2-[18F]fluoroethyl)-O-(p-nitrophenyl) methylphosphonate ([18F]VX surrogate),(James et al., 2014; Chao et al., 2016; Neumann et al., 2017) related OP tracers (Hayes et al., 2019), and also PET-labeled antidotes such as carbon-11–labeled 2-pyridine aldoxime methiodide (2-PAM) (Neumann et al., 2018).

Uniquely, [11C]POX is a PET tracer that covalently modifies targets in live tissues. To ensure that the radioisotope remained attached to targets and reports on this interaction, the carbon-11 radiolabel was strategically installed at the alkoxyl group of POX since the p-nitrophenol moiety is ejected (Fig. 1). This permits [11C]POX toxicokinetic and some pharmacodynamic measures to be evaluated in naïve and after unlabeled (nonradioactive, unlabeled) POX-injected challenge doses. Thus, the goal of this study was to prepare and administer [11C]POX to rats and then evaluate the radioactive biodistribution in rat blood and central and peripheral tissues. Herein, we describe the first radiosynthesis of [11C]POX and used in microPET imaging in rats as a means to evaluate the tracer CNS tissue penetration and radioactive distribution profiles correlated to blood and ex vivo tissue biodistribution (bioD) profiling.

Materials and Methods

General. Reagents and solvents such as dimethylformamide (DMF) and acetonitrile (CH_3CN) were reagent grade or better and were used without any additional purification (Sigma-Aldrich, Milwaukee, WI). USP-grade PBS, pH 7.4, was purchased from Sigma-Aldrich. Nuclear magnetic resonance (NMR) data were recorded in $CDCl_3$ or d_6-DMSO on a Bruker Avance 400-MHz spectrometer. High-performance liquid chromatography (HPLC) was performed with a Waters 590 system (Milford, MA) coupled to a Shimadzu SPD UV-Visible detector (Columbia, MD) and a gamma counting inline radiation flow detector (Model 105s; CRA, Berkeley, CA). The HPLC data were collected with an SRI PeakSimple Model 304 data system (Torrance, CA). Counting of tissue and blood samples used a Hidex automatic gamma counter (Turku, Finland). The PET and computed tomography (CT) imaging data were acquired using a Siemens Inveon microPET/CT scanner system (ca. 1.5 mm PET imaging spatial resolution). Male Sprague-Dawley rats (240–320 g) were used for imaging and biodistribution studies. The animals were cared for and used at the University of California, San Francisco (UCSF) facilities, which are accredited by the American Association for Accreditation of Laboratory Animal Care (AAALAC). The imaging and biodistribution studies were performed by adhering to UCSF Institutional Animal Care and Use Committee (IACUC)-approved protocols, which satisfied the National Institutes of Health guidelines and institutional regulations. Unlabeled paraoxon was synthesized as reported (Fletcher et al., 1950; Fagerlind et al., 1952) (Supplemental Fig. 1) and purified by column chromatography to >99%. *Caution:* paraoxon is highly hazardous and should be handled with gloves in a well-ventilated hood. Stored (neat) or aqueous/organic solutions of paraoxon can be destroyed by the addition of 1.0 N NaOH with overnight stirring at room temperature.

Synthesis of (HO)(CH₃CH₂O)P(O)(Oph$p$-NO₂). O-ethyl, bis-(O,O-p-nitrophenyl) phosphate (0.700 g, 1.9 mmol) was dissolved in

Fig. 2. Structure of [11C]POX and position of the carbon-11 label.

acetonitrile (5.0 ml) with stirring and mild warming. Once the solution became clear, 1.0 M NaOH (2.5 ml) was added dropwise over 30 minutes and the formation of hydrolyzed product was monitored by ^{31}P NMR and/or TLC (R_f ~0.05–0.10, CHCl$_3$:MeOH, 4:1) for 4 hours or until the starting material was consumed. The reaction was diluted with H$_2$O (25 ml) and extracted with CHCl$_3$ (2 × 25 ml) to remove remaining starting material, the aqueous layer acidified to pH 1.0–1.5 with 2.0 M HCl, and the product extracted with 3 × 25 ml CHCl$_3$: iPrOH (7:1). The organic layers were combined, extracted with saturated NaCl solution (40 ml), and stirred over anhydrous Na$_2$SO$_4$ for 24 hours. Filtration of solids and drying under high vacuum afforded the product O-ethyl, O-p-nitrophenyl phosphate monoacid (Krishnan et al., 1990) (251 mg, 53.7%) as a single P-31 NMR peak. Attempts to further purify the product by chromatography led to significant loss of material and, therefore, synthesis of this precursor was repeated multiple times. Spectral data: ^{1}H (400.18 MHz, CDCl$_3$) δ 10.25 (s, 1H); 8.22 (d, J = 9.1 Hz, 2H); 7.34 (d, J = 9.1, 2H); 4.21 (dq, J = 7.1, 1.1 Hz, 2H); 1.35 (dt, J = 7.1, 1.1 Hz, 3H). ^{31}P NMR (162.0 MHz, CDCl$_3$) δ −6.7.

Synthesis of (CH$_3$[^{11}C]CH$_2$O)(CH$_3$CH$_2$O)P(O)(Oph$p$-NO$_2$): [^{11}C]POX. [^{11}C]CO$_2$, produced by the ^{14}N(p, a) reaction on 1% O$_2$/N$_2$ on the GE PETtrace cyclotron at UCSF, was trapped on an aluminum tube charged with glass wool submerged in liquid nitrogen. A Teflon tube (100 cm, 0.030" I.D) was coated with a solution of 1.0 M MeMgBr (1 ml) in tetrahydrofuran (THF) at 0°C and partially dried by passing N$_2$ gas through it at 2 ml/min for 30 seconds. The [^{11}C]CO$_2$ was delivered through the coated loop using N$_2$ as a carrier at 8 ml/min. Once the activity was transferred to the loop, flow was shut off and the [^{11}C]CO$_2$ was allowed to react for 90 seconds at 0°C. A solution of 0.2 M LiAlH$_4$ (1 ml) in THF was used to elute the loop into a vial under a positive pressure of nitrogen. The solution was then dried starting at 80°C and raised to 120°C under a flow of N$_2$ (25 ml/min). After drying, the vial was cooled to room temperature and HI$_{conc}$ (0.35 ml) was added to afford CH$_3$[^{11}C]CH$_2$I. In a separate vial fitted with a septa cap, Cs$_2$CO$_3$ (10–12 mg) and O-ethyl, O-p-nitrophenyl phosphate (12 mg) were dissolved in DMF (0.4 ml). The CH$_3$[^{11}C]CH$_2$I was then placed in a 120°C heating block, and a distillation line containing P$_2$O$_5$ and ascarite traps was placed between the iodide and DMF vials. Using N$_2$ (25 ml/min) as a carrier gas, the temperature was increased to 180°C and distillation was performed for 5 minutes. The distillation lines were removed, and the reaction vial was then heated to 120°C for 5 minutes. Subsequently, the reaction was transferred directly for purification to a semipreparative HPLC using 1 ml of 5 mM phosphate buffer (PB, pH 6.8) to rinse the reaction vial. The desired peak was collected using a semipreparative column (t_R = 5.7 minutes, Luna C18(2) 250 × 10 mm, 50% PB pH 6.8, 50% MeCN eluent at 8 ml/min), and the resulting solution was diluted with 5-mM PB pH 6.8 (~25 ml) and passed through a preconditioned C-18 light Sep-Pak at a flow rate of 8 ml/min. The Sep-Pak was washed with PB (5 ml; 5 mM, pH 6.8), and the product, [^{11}C]POX, was eluted with acetonitrile (MeCN, 0.2 ml fractions) (Supplemental Figs. 2 and 3). The most concentrated MeCN fraction was diluted with 10 mM PBS (pH 6.8) to give a final concentration of ~10% MeCN, which was used for dosing. This [^{11}C]POX synthesis (Fig. 3) was completed on average within 40 minutes, yielding [^{11}C]POX in 10.3% ± 2.0% decay-corrected yield (n = 6, EOB; 40 minutes) with a molar activity of 4.96 ± 0.74 gigabecquerels (GBq)/μmol (134 ± 20 Ci/mmol). The typical yield for 55.5 GBq (1.5 Ci) of [^{11}C]CO$_2$ was 1.2–1.8 GBq (32–48 mCi) of [^{11}C]POX.
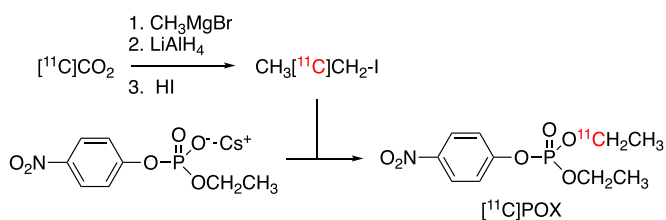
Fig. 3. Synthesis of carbon-11–labeled paraoxon [^{11}C]POX.

Arterial Sampling of Metabolites and Parent Tracers. Sprague-Dawley rats were anesthetized with isoflurane (1%–1.5%) and maintained under anesthesia for the duration of the procedure. An arterial catheter was placed at the upper region of the rat tail for blood sampling and flushed with a heparinized saline solution prior to blood collection. Bolus tracer doses (37–74 MBq, 1 to 2 mCi) were injected via tail vein catheter, and at 0.5, 1, 5, 10, 30, and 60 minutes, arterial blood (50–100 μl) was collected with heparinized syringes. Blood samples were placed in plastic 1.5 ml snap-lid centrifuge tubes preloaded with citric acid (25 μl of 10 mg/ml in sterile water). Each tube was centrifuged at 13,200 g for 1 minute at room temperature with a tabletop centrifuge, and the remaining supernatant was removed and placed in a second centrifuge tube. The red blood cell (RBC) pellet activity was counted (Hidex Automatic Gamma Counter). The supernatant was treated with 200 μl acetonitrile (equal volume to amount of blood volume used), and the tube was inverted a few times for ~0.5–1 minute and then centrifuged at 13,200 g for 1 minute at room temperature. The serum supernatant was separated from the serum protein pellet, and the pellet was counted. The serum supernatant was diluted with 200 μl distilled water and evaluated by analytical reversed-phase HPLC (Hamilton PRP-1, 5 μm, 250 × 4.6 mm, acetonitrile:10 mM phosphate buffer (pH 6.8) = 1:1, 1 ml/min, UV 254 nm, and radioactive detection). Two distinguishable fractions were observed: a hydrophilic fraction eluting at 2–5 minutes and a hydrophobic fraction eluting at 5–10 minutes. The fractions were collected, and radioactivity was counted (Hidex Automatic Gamma Counter). The data were exported from the Hidex instrument to Excel (Microsoft Corporation) software and reported as relative percentage (%) of total radioactivity, defined as the decay-corrected ratio of component radioactivity over the sum of all radioactivity counted across the samples × 100.

A sample of 100 μl formulated tracer [^{11}C]POX was processed using the same conditions as the arterial blood samples to assess stability. No breakdown of the tracer was found when assessed by radio-HPLC.

Biodistribution of [^{11}C]POX in Naïve Sprague-Dawley Rats. Sprague-Dawley rats were anesthetized with isoflurane (1%–1.5%) and were maintained under anesthesia with warming and constant monitoring throughout the experiment. A tail vein catheter was placed for injection of [^{11}C]POX (1.67–2.37 MBq/rat, n = 3 per time point). At 5 and 30 minutes after injection, blood (1–3 ml) was drawn by cardiac puncture followed by cervical dislocation and death confirmed by pneumothorax. Brain, liver, heart, kidney, and lung were excised and placed on absorbent paper, and specifically the heart was drained of excess blood. Blood and organs were weighed and radioactivity was counted after homogenization (decay corrected to the injection time) in the Hidex Automatic Gamma Counter. Percent injected dose per gram of tissue (% ID/g) was determined using a known radioactivity standard.

Calculated Estimates of Blood Activity in Rat Brain Tissues. Rat blood and brain tissue activity data over 1–30 minutes were analyzed to estimate the contribution of blood radioactivity of the total brain signal where the balance is in tissue radioactivity. Everett et al. (1956) previously demonstrated that average-sized rat brain blood volume is ~30–35 μl/g tissue. Using a midrange brain blood volume of 32.5 μl/g (equal to 0.0325 ml/g), and blood and brain % ID/g values per time point (Fig. 4) with a blood density of 1 g/ml, afforded the following relationships (eqs. 1 and 2) and ratio (eq. 3) where t = time point measured (for example at t_1):

$$\text{Blood at } t_1 (\% \, ID/g)$$
$$= blood \, \% \, ID/g \, at \, t_1 \times 1 \, g/mL \times 0.0325 \, mL/g \quad (1)$$

$$Brain \, at \, t_1 (\% \, ID/g) = brain \, \% \, ID/g \, at \, t_1 \quad (2)$$

$$Blood \, (\%) \, in \, brain \, tissue \, at \, t_1 (\% \, ID/g)$$
$$= blood \, at \, t_1 (\% \, ID/g) / brain \, at \, t_1 (\% \, ID/g) \times 100 \quad (3)$$

Rat MicroPET/CT and Magnetic Resonance Imaging. A dedicated small animal PET-CT (Inveon, Siemens Medical Solutions, Malvern, PA) was used for all imaging experiments. The magnetic resonance (MR) data, used for coregistration to the PET-CT data, were

Fig. 4. Baseline (naïve) rat arterial blood radioactivity component profiles ($n = 4$, decay-corrected) as a percentage of the total injected dose (% ID/ml; mean ± S.E.M.) vs. time (0.5–60 minutes) after intravenous injection of [^{11}C]POX. Data for red blood cells (RBC; -■■■-), plasma proteins (-●-), as diethylphosphoric acid metabolite (−π−), or as parent tracer (···■■■···). Inset shows a magnification of the 0- to 10-minute data.
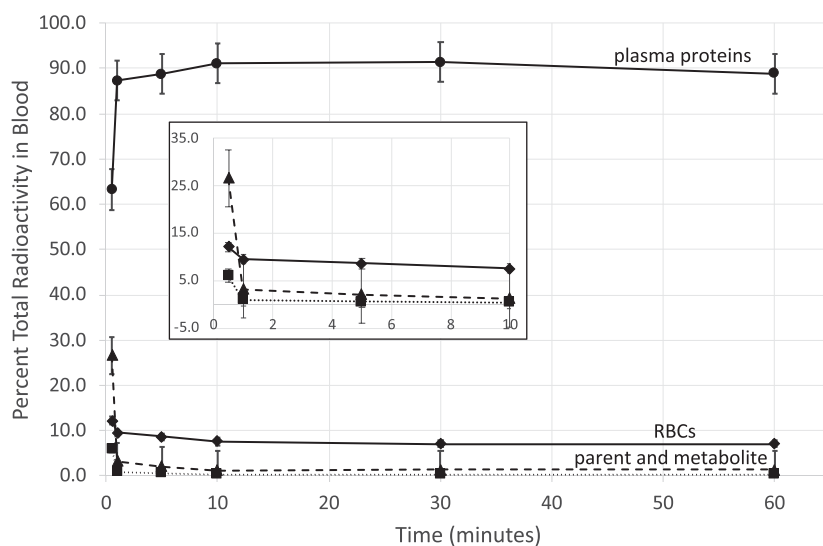
acquired with a Bruker BioSpin 7-Tesla magnet, using a multislice 2D FLASH protocol. For PET imaging, intravenous (i.v.) doses were formulated in 0.25–1.0 ml 10% acetonitrile/PBS (pH 6.8) and administered into anesthetized rats (1%–1.5% isoflurane) via slow bolus injections (18.5–74.0 MBq) into the tail vein via a catheter, followed by a 0.3-ml saline flush with PET-CT imaging following immediately thereafter. In other experiments, subcutaneous dosing conducted with [^{11}C]POX was formulated in 0.20 ml 10% acetonitrile/PBS (pH 6.8) administered between the shoulder blades (21.7–94 MBq) in anesthetized rats. Imaging was performed 10 minutes after injection for subcutaneous studies. The challenge PET imaging experiments with nonradioactive (unlabeled) POX blocking compound were accomplished by i.v. injection of unlabeled POX at 250 μg/kg (LD$_{50}$) in 10% acetonitrile/PBS (pH 6.8) (500–600 μl) at 20 or 60 minutes prior to tracer injection.

The PET-CT and MR imaging were performed northermic (37°C). Dynamic PET imaging data were acquired over 33 minutes (to meet the four to five half-life limit of radioactive decay) followed by 10 minutes for CT after tracer injection. The PET and CT data were reconstructed using Siemens vendor-provided software. An iterative reconstruction algorithm with CT-based attenuation correction was used for PET, and a Feldkamp reconstruction algorithm modified for conebeam was used for CT. The reconstructed volumes were 128 × 128 × 159 matrices with a voxel size of 0.776383 mm × 0.776383 mm × 0.796 mm for PET and 512 × 512 × 700 matrices with an isotropic voxel size of 0.196797 mm × 0.196797 mm × 0.196797 mm for CT. The CT acquisition parameters were: continuous 120 rotation steps over 220×, 80 kilovoltage peak (kVp)/500-μA tube using OSEM2D; as six frames, 300 seconds per frame for the 33-minute scans, decay time corrected, and quantified with a radiation phantom instrument calibration factor. A partial volume correction was not applied, and conservative region of interest (ROI) definitions were used as described further below. The multislice MR 2D FLASH protocol used the following parameters: T2*-weighted gradient recall echo, TR = 1528.3 milliseconds, TE = 7 milliseconds, and 256 × 256 × 50 voxels, affording 16 μm^3 resolution. The reconstructed PET-CT and MR imaging data were processed with AMIDE open-source software version 1.0.5 (Loening and Gambhir, 2003) and oriented as defined in Paxinos and Watson (2007).

The reconstructed MR, CT, and PET imaging data allowed for cranial landmarks of bregma and lambda to be identified from the CT images. The X, Y, Z coordinates of imaging views were centered at bregma, equivalent to the origin of the first scan, and then consistent landmark structures were iteratively coregistered and template fit against the cranial structures of the first scan landmarks. Subsequently, the landmarks were correlated with cerebral soft tissues from the MR scans.

The coregistered imaging data ROIs were defined as brain, heart, lung, kidney, and liver (Figs. 5–7) and defined within their volume

size limits and locations and against established stereotaxic three-dimensional locations (Walker and Homberger, 1997; Paxinos and Watson, 2007; Paxinos, 2015). PET scan regional tissue radioactivity is reported as standardized uptake value (SUV) defined as: [activity concentration in the tissue region of interest (MBq/cc)/decay-corrected injected dose at time = 0 (MBq)] × body weight of the rat as grams (g) (Gambhir, 2004). ROI PET scan statistics (SUV ± S.E.M.) collected from time points at midframe were exported to Excel (Microsoft Corporation), and plots of SUV versus time were generated using Excel. Integration of areas under the SUV curves (AUCs) was performed with R (Version 3.5.2). One-way ANOVA, post hoc Tukey honestly significant difference (HSD) comparison, and Student's t test were performed using Microsoft Excel (Version 16.16.12) or R (Version 3.5.2). A P value < 0.05 was considered statistically significant.

Results

Radiosynthesis of [^{11}C]POX (Fig. 3). Prior nonradioactive syntheses of POX (Mastin et al., 1945; Fletcher et al., 1950; Fagerlind et al., 1952) were not amenable to radiolabel introduction; therefore, the synthesis of [^{11}C]POX (Fig. 3) was conducted similarly to the carbon-11–labeled VX-analog previously described (Hayes et al., 2021). In brief, [^{11}C]CO$_2$
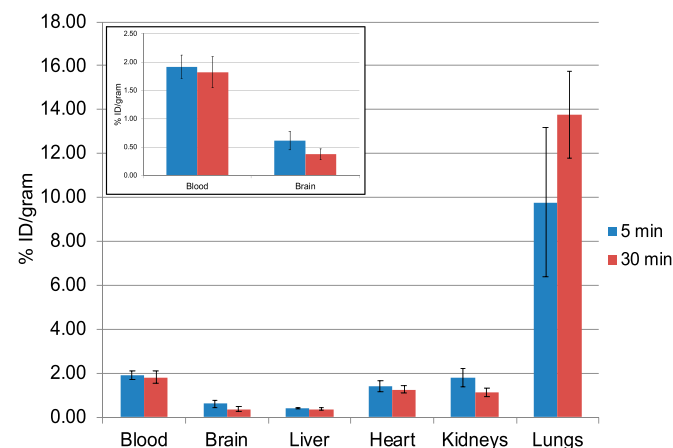
Fig. 5. Biodistribution of [^{11}C]POX in rat blood and select tissues at 5 and 30 minutes after intravenous injection. Inset: expansion of the blood and brain distributions.
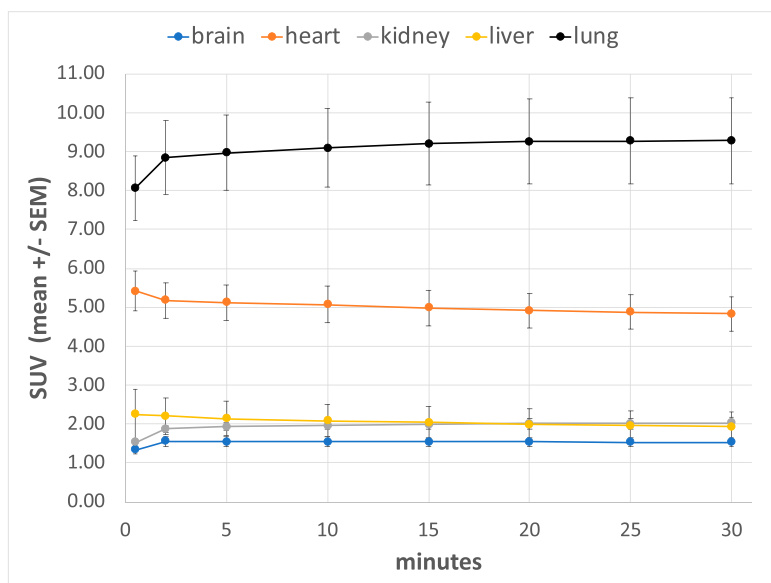
Fig. 6. Time-activity curves in tissues of naïve rats after intravenous administration of [¹¹C]POX.

was reacted with CH_3MgBr, reduced with $LiAlH_4$ to form $CH_3[^{11}C]CH_2OH$, and converted to $CH_3[^{11}C]CH_2$-I using hydroiodic acid. The radiolabeled reagent, $CH_3[^{11}C]CH_2$-I, was coupled with the cesium salt of O-ethyl, O-p-nitrophenyl phosphoric acid (Krishnan et al., 1990) to yield [¹¹C]POX in 10.3% ± 2.0% decay-corrected yield (n = 6, EOB; ∼40 minutes) with a molar activity of 4.96 ± 0.74 GBq/μmol (134 ± 20 Ci/mmol). As noted, placement of the [¹¹C]label at the ethoxy group retains radioactivity on adducted phosphylated targets after loss of the p-nitrophenoxy group.

Baseline Blood Evaluation of [¹¹C]POX in Naïve Rats. Arterial blood sampling was conducted at 0.5, 1, 5, 10, 30 and 60 minutes to evaluate the radioactivity associated with [¹¹C]POX (parent), the principal metabolite [¹¹C]diethylphosphoric acid (Erdos and Boggs, 1961; Nakatsugawa et al., 1969), plasma proteins, and red blood cells (RBCs) (Fig. 4) after the [¹¹C]POX tracer was given as an intravenous (i.v.) dose. The carbon-11 half-life of 20 minutes limited analyses to ∼60 minutes after injection

but were inclusive of 5- and 30-minute sampling time points to correlate with the ex vivo bioD tissue sampling. By 1 minute, a reduction in the amount of [¹¹C]POX parent tracer to <1% was observed along with a corresponding increase in radiolabeled plasma proteins (∼87%) and RBCs (∼9%).

The [¹¹C]POX parent levels remained at 1%–5% over the 60-minute experimental duration, whereas the protein fraction remained high at 80%–90% and the RBC fraction leveled out at about 7%. The principal metabolite [¹¹C]diethylphosphoric acid (validated by comparison with authentic material) (Erdos and Boggs, 1961; Nakatsugawa et al., 1969) was >20% of the total radioactivity in blood by the first minute but decreased to 1%–3% although with variability. The immediate formation of the metabolite [¹¹C]diethylphosphoric acid is likely due to the breakdown of [¹¹C]POX in blood by enzymes and/or hydrolysis; however, rapid, stepwise protein adduct formation and concomitant ejection of [¹¹C]diethylphosphate from these adducted proteins also contribute to the net
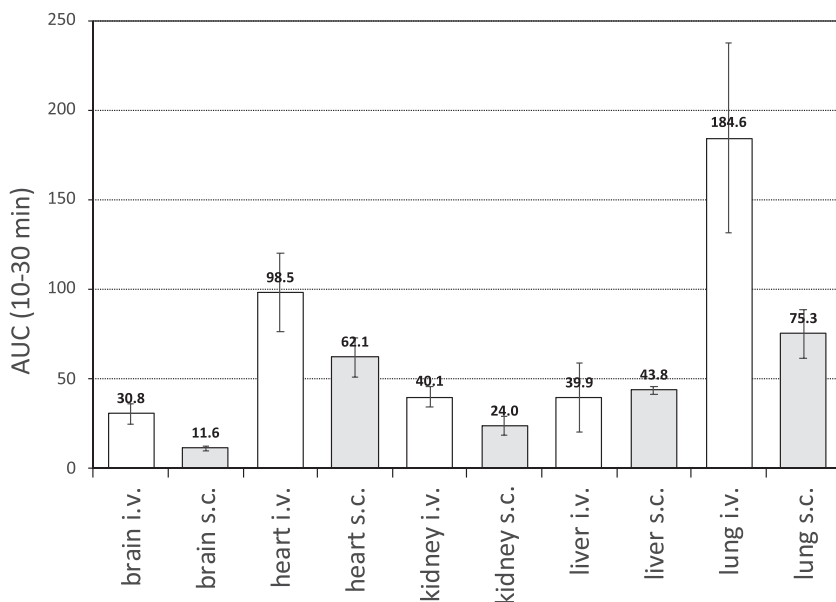
Fig. 7. Comparison of intravenous (unfilled bars) and subcutaneous (filled bars) tissue distributions from 10 to 30 minutes. Mean area under the curve (AUC) values shown above each bar.

radioactivity levels both in the early phase and over the 60-minute time course of the blood sampling. The persistently high radioactivity levels in the protein fraction likely correlate with covalent tracer phosphorylation of carboxylesterases (Maxwell, 1992; Dettbarn et al., 1999) and other serum esterases not associated with blood cells. The RBC fraction shows a steady radioactivity level over 60 minutes due to tracer attachment to surface-anchored AChE, although passive RBC penetration by intact [^{11}C]POX is also possible. Since very low tracer mass levels were given (~200 ng), the arterial blood levels demonstrate that [^{11}C]POX quickly reacted in blood with the large surplus of serum proteins and RBCs, resulting in [^{11}C]diethoxyphosphoryl adducts. Still, a very small circulating free fraction of [^{11}C]POX that did not react with blood proteins and cells would be available to enter tissues. This process could be assessed by biodistribution studies in which [^{11}C]POX tracer is given and radioactivity levels are measured in various tissues.

Ex Vivo Biodistribution Measures in Naïve Rats: Intravenous [^{11}C]POX Administration. The baseline ex vivo bioD radioactivity profiles were determined in naïve rats from whole blood (unfractionated), brain, liver, heart, and kidney at 5- and 30-minute time points after an intravenous [^{11}C]POX tracer injection. Baseline blood evaluations showed a rapid decrease in parent [^{11}C]POX tracer within 1 to 2 minutes; therefore, bioD measures were conducted at 5 and 30 minutes, in which the 5-minute data would reflect tracer distribution after the initial reaction period (Fig. 5, inset) and the 30-minute time would represent a time point where radioactivity changes would be minimal. The data were obtained as decay-corrected percent injected dose (ID) radioactivity standardized as per gram tissue values (% ID/g) ± standard error (S.E.M.) (Fig. 5).

Lung showed the highest radioactivity values at 5 minutes and 30 minutes with ~10% ID/g and 15% ID/g, respectively. Approximately 2% ID/g uptake was in blood and 1% to 2% in heart and kidneys each. Brain and liver had less than 1% ID/g radioactivity. Blood levels did not change significantly (5 minutes vs. 30 minutes) indicating that most reactions with [^{11}C]POX had completed by 5 minutes (Fig. 5, inset). Most tissues decreased in radioactivity from 5 to 30 minutes except lung. The larger levels in lung at 30 minutes were attributed to elevated amounts of carboxylesterases found in rat lung tissue and similar to a previous finding using a fluorine-18 OP tracer (Hayes et al., 2020, 2021; Thompson et al., 2020). As expected, heart radioactivity levels closely paralleled blood levels at both the 5- and 30-minute time points. It is thought that the larger fraction of blood, serum, and lung proteins phosphorylated by [^{11}C]POX offsets the lower radioactivity levels found in kidney and liver. Higher kidney levels might have been expected based on accumulation of the nonreactive, water-soluble metabolite [^{11}C]diethylphosphoric acid levels found in blood, but this was not observed.

Radioactivity was found in brain at both the 5- and 30-minute time points (Fig. 5, inset) despite very little, if any, [^{11}C]POX tracer remaining in blood after 1 minute (Fig. 4). Brain radioactivity levels were about 32% of the blood radioactivity at 5 minutes and 20% of blood levels at 30 minutes. The brain radioactivity levels at 5 minutes are presumably a combination of unreacted, free parent [^{11}C]POX and [^{11}C]POX-modified protein targets in brain, whereas the radioactivity at 30 minutes reflects steady levels of [^{11}C]POX-modified proteins after washout of the free tracer. If the average rat brain blood volume is approximately 30–35 μl/g tissue (Everett et al., 1956), the blood and brain % ID/g values indicate that about 14% (8%–20%) of the brain radioactivity is due to cerebral blood. Assuming any unreacted parent tracer had undergone cerebral efflux, the majority (~86%) of the brain radioactivity is associated with [^{11}C]POX-modified protein targets. Given the extremely low injected nanogram dose of [^{11}C]POX (~200 ng) coupled with the rapid decline in blood and increase in plasma protein conjugates, it was unanticipated that substantive levels of [^{11}C]POX would be available to enter brain and modify proteins. An important conclusion from this experiment is that POX exposures, even at nanogram to picogram levels, may result in some fraction of POX entering brain and reacting with susceptible proteins.

Baseline PET Imaging Biodistribution Determinations in Naïve Rats via [^{11}C]POX Intravenous Injection. Radioactivity biodistributions using PET imaging were conducted in naïve rats to determine the dynamic in vivo tissue radioactivity profiles after [^{11}C]POX injection. The radioactivity levels in rats were determined as SUV to enable comparisons across time (Gambhir, 2004) where radioactivity profiles in heart, lung, kidney, liver, and brain were determined (Fig. 6; $n \geq 3$ per tissue). For comparative appraisal, the in vivo imaging time-activity curve (TAC) duration was conducted similarly to the ex vivo bioD time points, *vide infra*.

Naïve rats injected with [^{11}C]POX had the highest initial radioactivity SUV values in lung and heart tissue that persisted over 30 minutes, leveling to SUV values of ~ 9.0 and 5.0, respectively (Fig. 6). The liver and kidney SUVs were ~2.0 and were maintained over the experiment timeframe, with most changes occurring in the first few minutes. Brain had the lowest tissue levels overall (SUV ~1.5), but the level persisted in radioactivity over 30 minutes. Although the TACs differ from the ex vivo bioD data, the trends were similar (e.g., lung tissue had the largest fraction of radioactivity in both studies). Heart tissue revealed a far greater amount of radioactivity (>50%) relative to lung per the TAC PET values compared with the ex vivo bioD in which both 5- and 30-minute time points were only 10%–15% relative to lung.

Kidney and liver were nearly identical and lower than lung in the TAC PET experiments, although kidney was higher in the ex vivo bioD analysis. In both sets of experiments, brain tissue gave the lowest levels of radioactivity that stabilized over 30 minutes. Both the PET imaging and bioD studies revealed steady, elevated brain SUV levels over 30 minutes without significant radioactivity washout that is likely due to the covalent modification of proteins by OPs in the CNS.

Baseline PET Imaging Biodistributions Determined in Naïve Rats via [^{11}C]POX Subcutaneous Injection. To assess possible differences in naïve rats due to the route of administration, the [^{11}C]POX tracer was given by subcutaneous (Turner et al., 2011) injection. The subcutaneous route more closely models some occupational exposure in humans as reported for diisopropyl fluorophosphate (DFP) (Rojas et al., 2020), chlorpyrifos (Voorhees et al., 2019), and other OPs (Voorhees et al., 2017). Rats were dosed via subcutaneous injection with [^{11}C]POX with a molar activity range similar to that used for the intravenous [^{11}C]POX experiments to minimize differences in the POX dose mass and to compare AUC levels as a function of time. The tissue-accumulated AUC values were determined from 10 to 30 minutes after subcutaneous injection

(Fig. 7). The initial subcutaneous AUC measures were conducted at 10 minutes to compensate for the slower rate of diffusion from the injection site and obscuring of certain tissues. After subcutaneous [^{11}C]POX injection, lung and heart tissue showed the largest tracer AUC values (Fig. 7), followed by liver and kidney, with brain affording the lowest overall AUC values.

When compared with the intravenous injection route, subcutaneous injection led to lower AUC values in most tissues (except liver), whereas the remaining overall AUC trends appeared similar. AUC brain levels determined for intravenous administration of [^{11}C]POX were almost 3-fold that of the subcutaneous route. To more critically evaluate the difference between intravenous- relative to subcutaneous-administered CNS tissue radioactivity profiles, brain:tissue AUC ratios were determined (Fig. 8). In this evaluation, the brain:heart and brain:lung ratios were highly similar for both injection routes. The brain-to-liver ratios were complicated by large statistical errors in the intravenous liver data; however, the brain-to-liver subcutaneous AUC ratio aligned well with the other data (Fig. 8).

Arterial Blood Sampling Evaluation: Naïve versus Nonradioactive POX Pretreatment Challenge. The amount and composition of radioactivity in blood was determined at 20- and 60-minute time points with [^{11}C]POX tracer after an LD$_{50}$ dose (250 μg/kg) of nonradioactive POX had been given. Changes in the parent [^{11}C]POX, radioactive metabolite (diethoxyphosphate), and radioactivity associated with red blood cells (RBCs) and serum proteins (Fig. 9) due to the nonradioactive POX challenge dose were determined. The 20-minute time point was selected because it coincides with extensive in vivo inhibition of AChE by POX and corresponding neurotoxic action (Worek et al., 2011). By 60 minutes the initial POX toxidrome decreases and the radioactivity levels would provide insights into the recovery process, although reactivation levels of POX-modified proteins would not be significant. OP-induced seizures are suppressed in animals treated with isoflurane (Krishnan et al., 2017), but the overall mechanism of POX action is retained. Overall, rats were dosed with an LD$_{50}$ POX dose (250 μg/kg), and in separate experiments the [^{11}C]POX tracer was given at 20 or 60 minutes, whereupon the radioactivity in

the blood fractions was measured at 0.5, 1.0, 5.0, 10.0, and 30.0 minutes after tracer injection (Fig. 9).

The percentage (%) of total radioactivity for the four blood fractions after unlabeled POX (250 μg/kg) at 20 minutes differed significantly from the parent tracer in naïve experiments (Fig. 4) and the 60-minute time point (Fig. 9). These differences reflect the maximal inhibition of proteins by nonradioactive POX at 20 minutes at the high (LD$_{50}$)-dose level. At 20 minutes, a large number of OP-reactive enzymes are inactivated by the nonradioactive POX, and subsequently when [^{11}C]POX is administered, the tracer cannot attach to blocked proteins and radioactivity is far less bound, consumed, or converted by target proteins. For example, parent [^{11}C]POX levels determined at 20 minutes after unlabeled POX treatment were several-fold higher than naïve (tracer only) or at the 60-minute post-POX time point. However, toward the end of scanning at 30 minutes, the parent radioactivity levels were similar for all treatment groups.

When [^{11}C]POX was given 20 minutes after unlabeled POX treatment, the radioactivity profiles reflect complementary changes in blood component radioactivity. For example, in the first 10 minutes, [^{11}C]POX (parent) tracer steadily decreases with a corresponding increase in radiolabeled plasma proteins. This suggests that at 20 minutes many blood protein targets have been bound or blocked by unlabeled POX such that a greater amount of the [^{11}C]POX parent tracer can survive the first 10 minutes of blood circulation (Fig. 9) and correspondingly that this [^{11}C]POX free fraction is available to react with plasma proteins, resulting in an increase in protein radioactivity from 30% to 60%. The protein levels at 20 minutes (Fig. 9) remained 15%–25% lower than naïve or 60-minute time point and could be due to sustained phosphorylation of carboxylesterases (Maxwell, 1992; Dettbarn et al., 1999).

The level of POX metabolite (Erdos and Boggs, 1961) [^{11}C]diethylphosphoric acid (Nakatsugawa et al., 1969) was highest 20 minutes after unlabeled POX was given and stabilized at ~15% of the blood component radioactivity. This amount was 5-fold greater than what was found in either the naïve rats or in rats 60 minutes after POX was given. For the 20-minute time point, the RBC fraction showed 20% of the total radioactivity or about twice the levels found in the
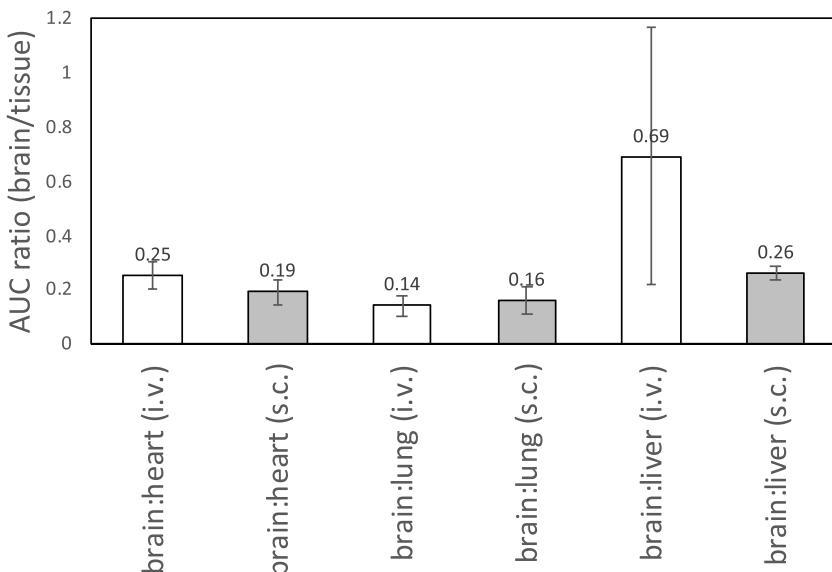
Fig. 8. Comparison of intravenous and subcutaneous brain:heart, brain:lung, and brain:liver AUC ratios ($n = 3$).
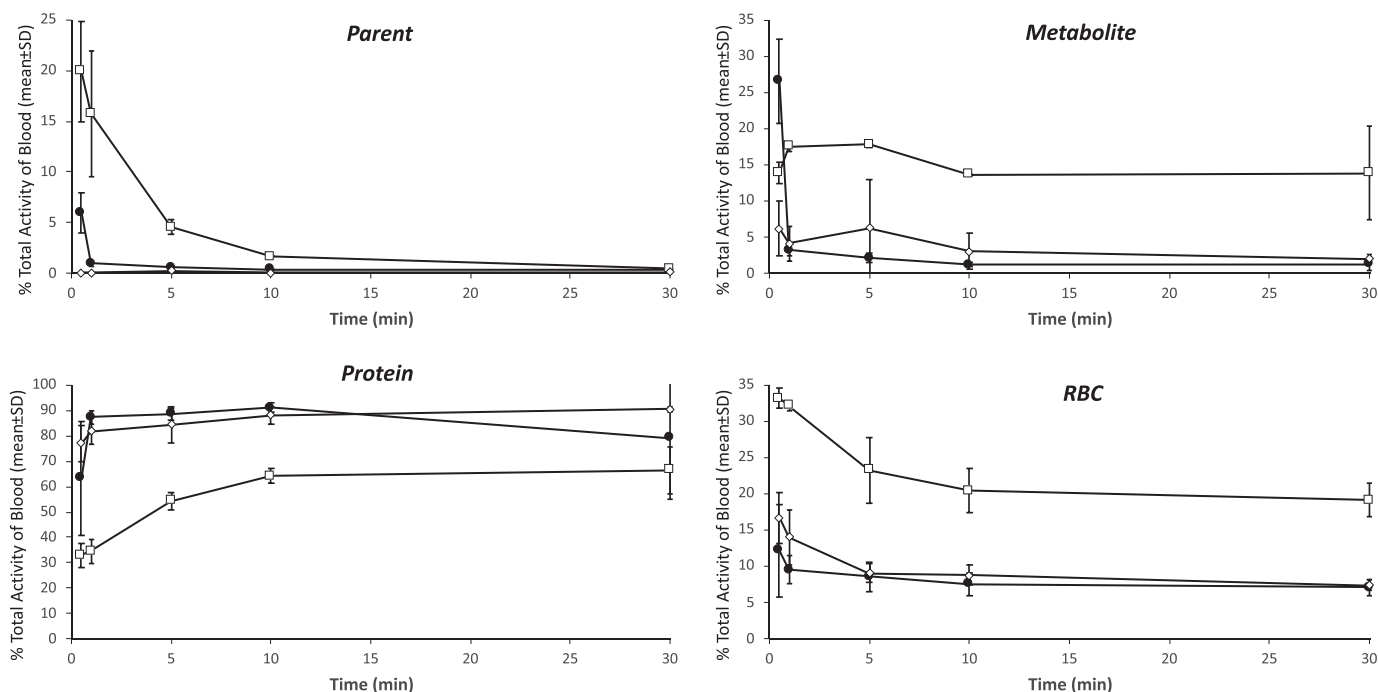
Fig. 9. Comparison of the rat blood radioactivity in naïve (tracer only) and 20 and 60 minutes after nonradioactive POX pretreatment, where ● = naïve i.v.; □ = POX 250 μg/kg, 20 minutes; and ◇ = POX 250 μg/kg, 60 minutes.

naïve and 60-minute studies. Since the total percent radioactivity of plasma proteins is reduced by ~20% when nonradioactive POX is given 20 minutes prior to tracer (Fig. 9), it is possible that the increased available fraction of [^{11}C]POX modifies a proportionally greater amount of the RBC proteins.

Although parent, metabolite, protein, and RBC radioactivity levels for the naïve and at 60 minutes after nonradioactive POX dosing were similar, differences observed at 0.5 minutes may be due to variation in the injection, volume, and/or diffusion rate from the injection site. Additionally, a direct effect of nonradioactive POX pretreatment on parent [^{11}C]POX levels cannot be dismissed. The key similarities in the [^{11}C]POX only (naïve) and 60 minutes after nonradioactive POX pretreatment suggest that by 60 minutes, the initial nonradioactive-induced changes to blood components have recovered to near naïve-like levels. This is particularly evident in the serum protein and RBC fractions that show similar radioactivity values over the 30-minute sampling period, which implies that comparable serum butyrylcholinesterase (BChE) and RBC AChE activities are present in blood of the naïve and at 60 minutes after an LD$_{50}$ dose of nonradioactive POX.

In sum, rats given unlabeled POX 20 minutes prior to tracer led to the most significant changes in the blood component radioactivity profiles because they likely correlate to peak inhibition of AChE by POX. By 60 minutes after an LD$_{50}$ pretreatment dose of nonradioactive POX, the blood component tracer profiles showed target recovery as revealed by radioactivity levels more closely aligned with those found in the naïve tracer studies. Although the peak changes in blood profile occurred at 20 minutes after POX was given, such changes may differ for OP other than POX.

PET Imaging Tissue Activity Distributions with [^{11}C]POX after an Unlabeled (Nonradioactive) POX LD$_{50}$ Pretreatment Dose. Tissue tracer uptake profiles were evaluated using PET imaging with [^{11}C]POX at the 20- and

60-minute time points after pretreatment with unlabeled POX (LD$_{50}$), similar to the arterial blood sampling. These tissue PET imaging data acquisitions were analogous to the imaging assessments in naïve rats and were conducted by intravenous tracer injection. Heart, lung, liver, and brain tissue radioactivity distributions were determined (Fig. 10); however, kidney profiles were not consistent due to the limited field of view based on rat placement in the scanner and were omitted from analyses. The tissue radioactivity profiles were expressed as mean area under the curve (AUC) values and standard deviation (S.D.) at 20 and 60 minutes after POX was given (Fig. 10). The AUC data were taken from 10- to 30-minute time-activity curves where steady radioactivity values were realized. The variable and potentially confounding statistical fluctuations from the early uptake (1–10 minutes) were not included in the AUC determinations. One-way ANOVA analyses of the 10- to 30-minute AUC values between the absence (naïve) versus 20- or 60-minute pretreatment dosing with 250 μg/kg nonradioactive POX (challenge, blocking), as a function of tissue and blood, showed significant differences.

The tissue profile data revealed that brain, heart, and lung showed decreases in AUC levels at the 20-minute unlabeled POX challenge time versus naïve, whereas the 60-minute time assessment revealed partially recovered AUC radioactivity levels approaching naïve values (Fig. 10). For example, the brain AUC = 30.8 in naïve rats, but at 20 minutes after unlabeled POX blockade brain AUC = 8.8 and at 60 minutes brain AUC = 25.3 (>80% of naïve). Heart and lung AUCs also recovered but not nearly to the level of brain at 60 minutes. AUC levels were heart = 98.5 and lung = 184.6 in naïve rats, but 20 minutes after unlabeled POX was given, these tissue radioactivity levels had dropped to 17.6 and 17.3, and then by 60 minutes the levels recovered to AUC = 51.1 and 53.2, respectively. Although the heart and lung AUC levels recovered, the AUCs restored to only 25% and 50% of the naïve AUC
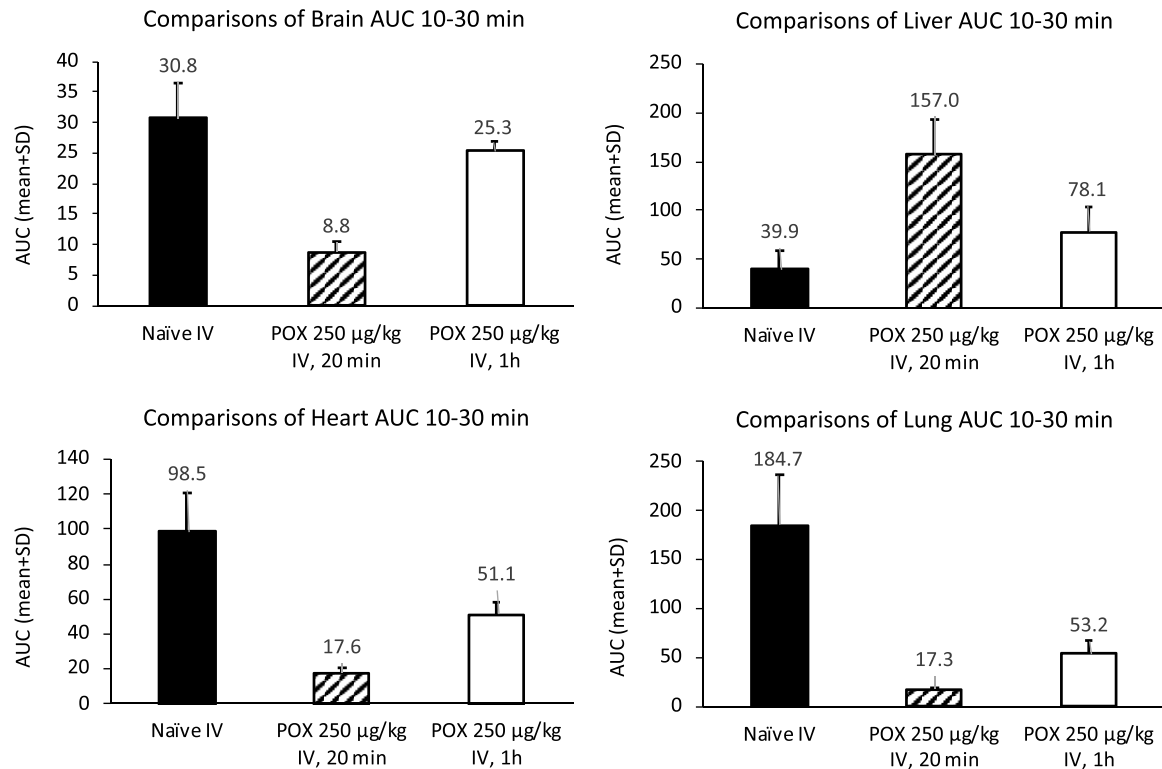
Fig. 10. Comparison of tissue distribution (AUC) in naïve (A) and nonradioactive POX- pretreated rats at 20 minutes (B) and 60 minutes (C). ANOVA P values: brain, 0.00044; heart, 0.00022; liver, 0.00040; lung, 0.00036. Post hoc Tukey honestly significant difference (HSD) P value < 0.05; brain: (A) vs. (B), (B) vs. (C); heart: (A) vs. (B), (A) vs. (C); liver: (A) vs. (B), (B) vs. (C); lung: (A) vs. (B), (A) vs. (C).

levels, respectively. Additionally, the magnitude of the 60-minute recovery time point is also apparent in the related blood profiles (e.g., Fig. 10 vs. Fig. 9). In heart and lung, either [^{11}C]POX activity had washed out and/or nonradioactive POX-modified enzymes had partially reactivated after 60 minutes relative to the respective 20-minute AUC levels.

Liver AUC levels at 20 minutes after POX differed from brain, heart, and lung and increased 4-fold from 39.9 (naïve) to 157.0 (20 minutes) and then decreased to 78.1 at 60 minutes (Fig. 10). For liver, the increased 20-minute AUC level may represent tracer metabolite levels and [^{11}C]POX-modified proteins resulting from a greater amount of available [^{11}C]POX tracer after nonradioactive POX had blocked blood enzymes. This premise agrees, in part, with the arterial blood studies (Fig. 9) in which tracer metabolite levels

were 7- to 8-fold higher at 20 minutes after nonradioactive POX pretreatment. Comparisons of mean value AUC ratios such as brain/heart and brain/lung were also made (Fig. 11). Comparison of the more variable naïve ratios (e.g., elevated error bars) to the 20- and 60-minute brain/heart and brain/lung ratios revealed that the nonradioactive POX-pretreated 20- and 60-minute AUC ratios were both elevated relative to naïve AUC ratio levels. The elevated 20-minute versus 60-minute pretreated AUC ratios were found to be indistinguishable from each other.

Time-activity curves were also determined in rats using [^{11}C]POX to probe six brain subregions (cerebellum, caudate putamen, brainstem, thalamus, midbrain, and frontal cortex) in naïve, 20- and 60-minute after nonradioactive POX injection (Fig. 12).
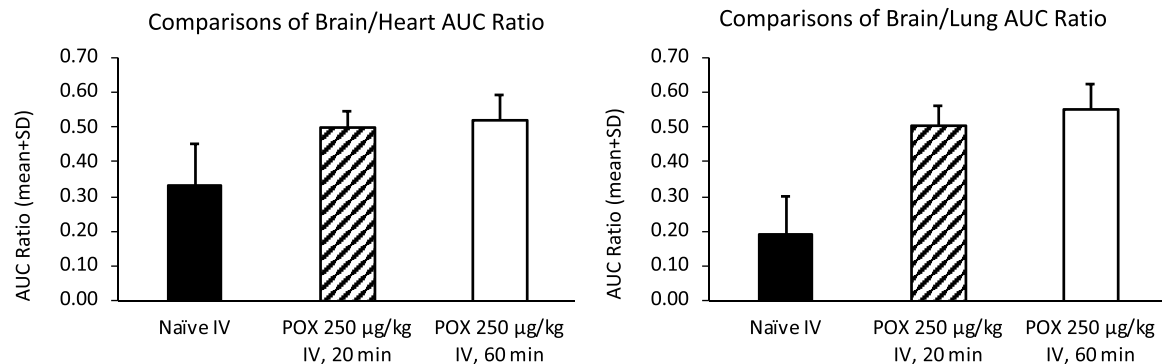
Fig. 11. Brain:heart and brain:lung AUC ratios for naïve (devoid of nonradioactive POX pretreatment) and at 20 and 60 minutes after nonradioactive POX pretreatment given at 250 μg/kg).

[^{11}C]POX Levels in Select Brain Regions

[^{11}C]POX Levels in Select Brain Regions 20 min after LD$_{50}$ POX

[^{11}C]POX Levels in Select Brain Regions 60 min after LD$_{50}$ POX
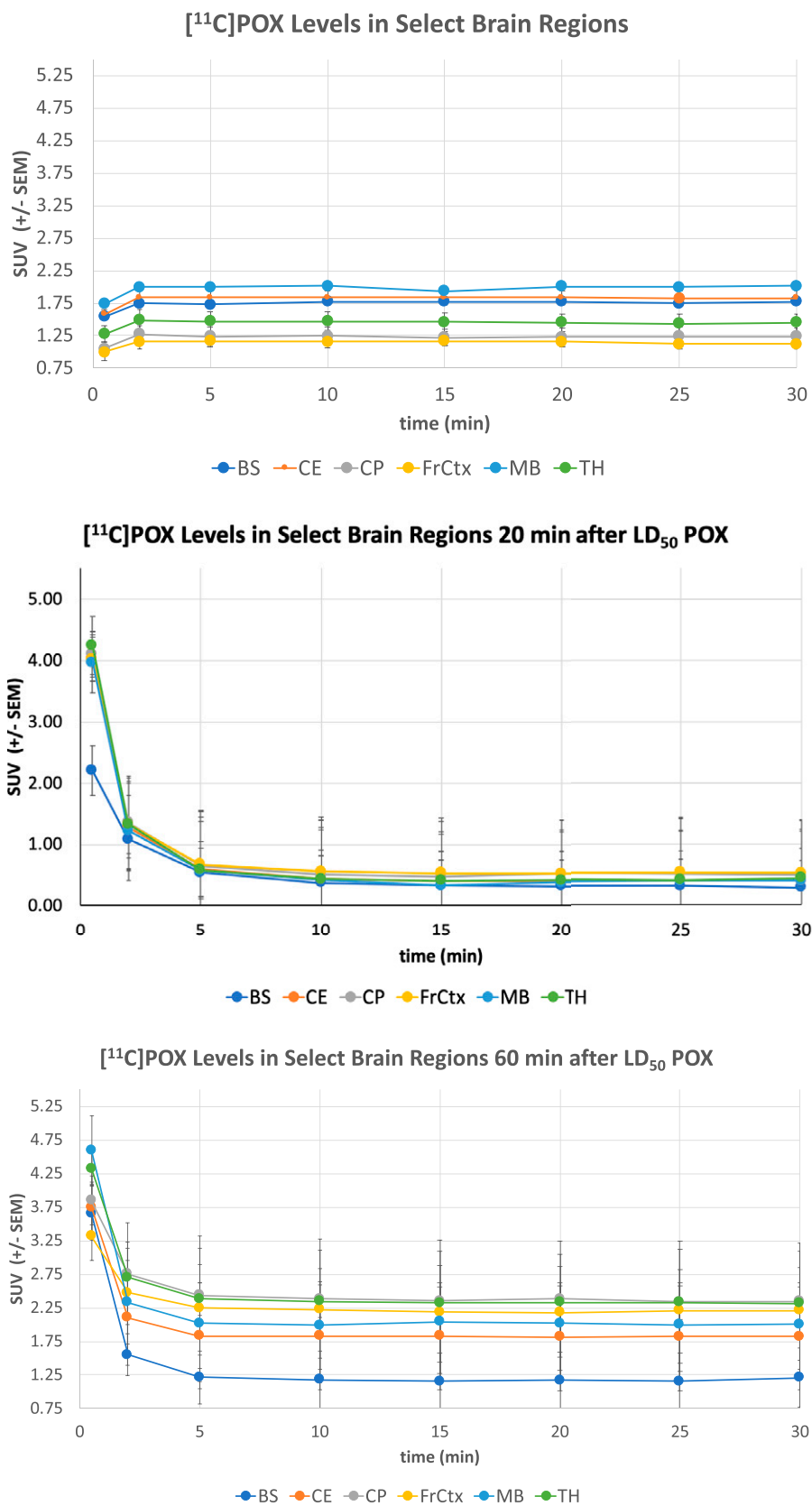
Fig. 12. Brain region SUV levels for naïve (top) (no unlabeled POX), at 20 minutes (middle), and at 60 minutes (bottom) after nonradioactive POX pretreatment given at 250 μg/kg.
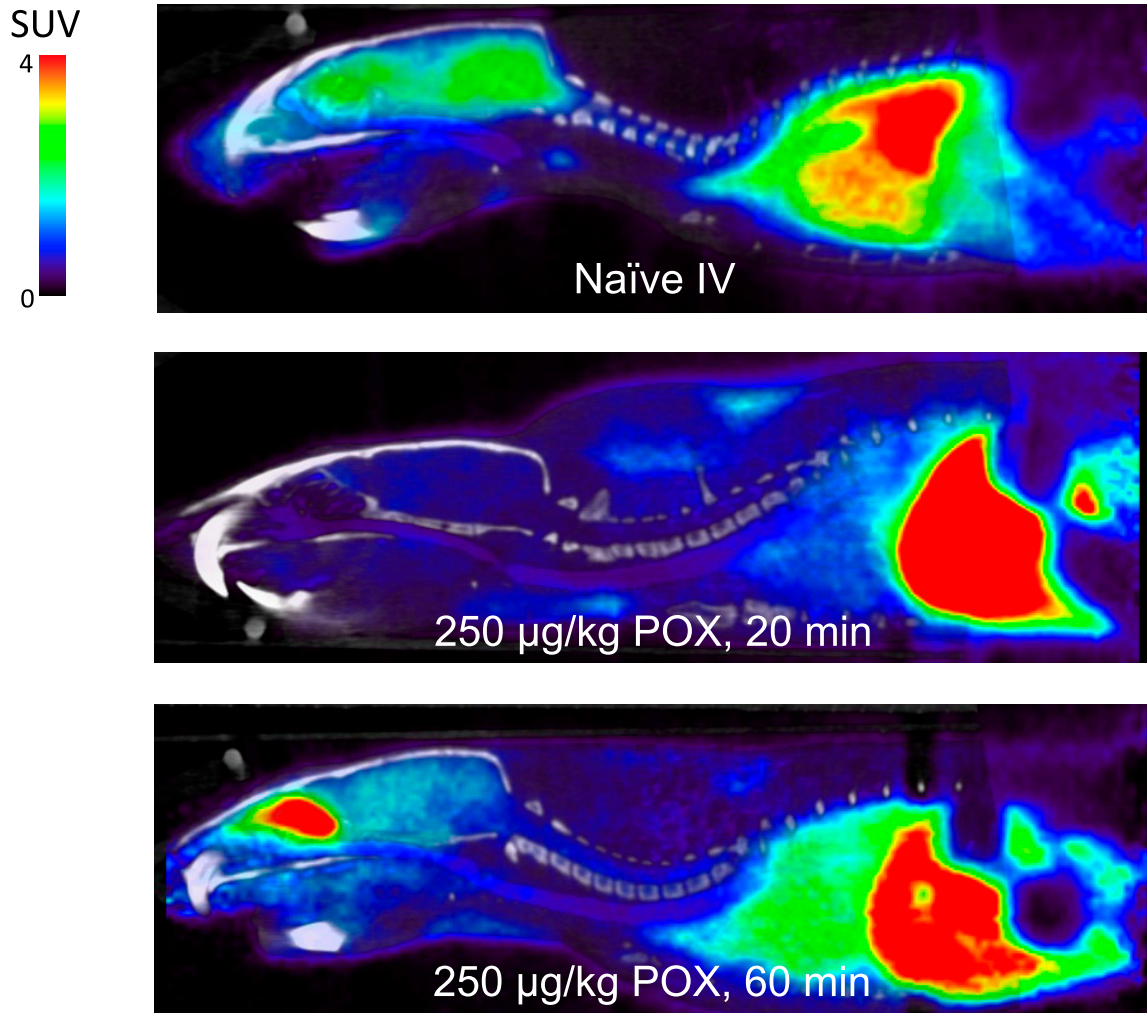
Fig. 13. PET imaging of rats treated with [^{11}C]POX only (naïve) and [^{11}C]POX at 20 minutes and 60 minutes after an LD$_{50}$ dose of nonradioactive POX.

In naïve rats, each of the six brain regions revealed similar trends (i.e., with an initial small rise in radioactivity in the first 1 to 2 minutes followed by apparent stable activity levels over 30 minutes). Midbrain afforded the highest radioactivity levels (SUV $\sim$ 2.0) and frontal cortex the lowest (SUV $\sim$ 1.1). There was no apparent radioactivity tissue washout by the end of imaging that correlates with covalent modification of brain target proteins. Rats given [^{11}C]POX 20 minutes after nonradioactive POX (LD$_{50}$) showed a rapid decrease from initial radioactivity levels at 1 minute (SUV 2.2–4.2) to 4- to 7-fold lower levels (SUV 0.54–0.67) at 5 minutes and then leveled out for the balance of the imaging time. The initial high radioactivity in brain and subsequent activity leveling is indicative of rapid [^{11}C]POX CNS influx, but when most targets are blocked by nonradioactive POX pretreatment, the PET tracer is unable to modify OP-susceptible proteins lowering radioactivity levels in CNS compared with naïve. The residual radioactivity levels are presumably a sum of covalently modified functional protein targets that did not react with nonradioactive POX.

At 60 minutes after nonradioactive POX (LD$_{50}$) treatment, rats given [^{11}C]POX showed radioactive SUV levels higher than the 20-minute levels. In two instances (cerebellum, midbrain), the brain region radioactivity levels were identical to

naïve after 5 minutes, possibly indicative of radioactivity washout. Some brain regions in the 60-minute treatment group, however, retained radioactivity levels even higher than naïve rat levels. Although there was statistical variability, the mean value radioactivity stayed higher (up to 2-fold) and sustained in these brain regions compared with naïve rats. This suggests that more [^{11}C]POX entered brain and subsequently modified a greater number of target proteins in the caudate putamen, frontal cortex, thalamus, and brainstem regions. This may be due to the high pretreatment dose of nonradioactive POX resulting in inhibition and/or modification of blood proteins that remain blocked, thereby allowing in a greater availability of [^{11}C]POX tracer to survive and enter brain. A second possibility is changes in blood-brain barrier permeability due to POX toxicity that could allow more [^{11}C]POX tracer to enter brain.

[^{11}C]POX tracer only given to naïve rats represents an extremely low-mass dose of POX of $\sim$200 ng). Pretreatment with nonradioactive POX at the LD$_{50}$ followed by [^{11}C]POX tracer administration would be expected to change the CNS radioactivity levels because OP-sensitive enzymes such as AChE, butyrylcholinesterase (BChE), and lung carboxyesterases would be blocked in part or in full. The nonradioactive POX enzyme blockade allows [^{11}C]POX to elude attachment to these enzymes, and
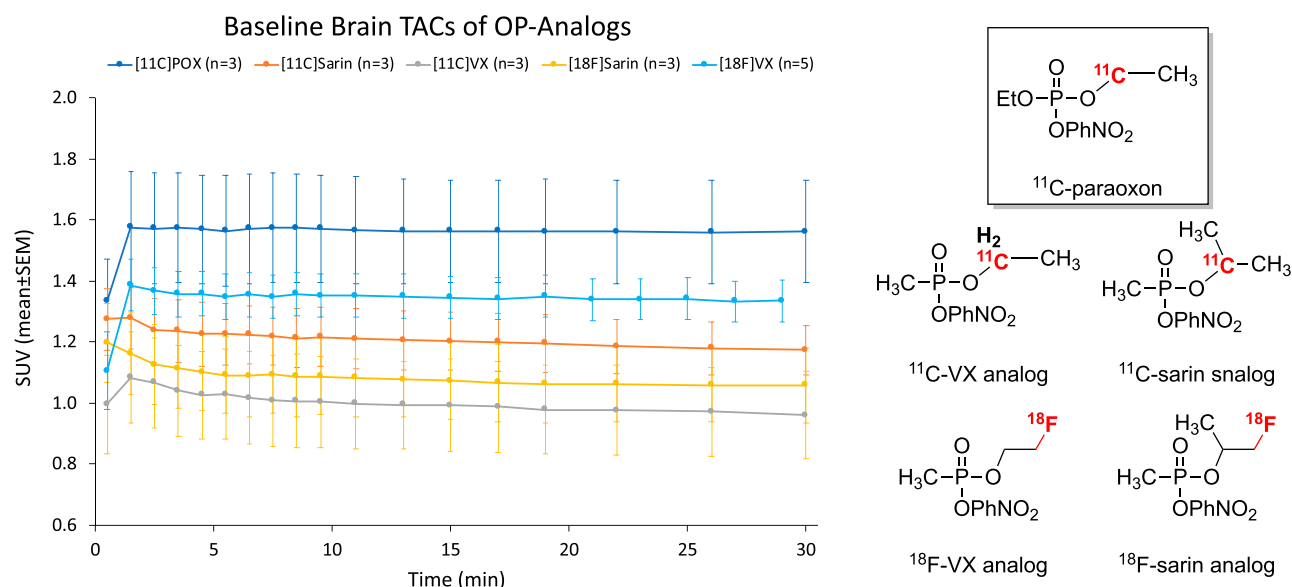
Fig. 14. Comparison of PET imaging male rat brain 0- to 30-minute time-activity curves (TACs) for five different OP PET tracers after intravenous tracer injections.

a greater amount of tracer could enter the CNS. However, the far larger dose of nonradioactive POX given can also modify CNS enzymes, and although more [^{11}C]POX tracer can enter brain from the bloodstream, fewer brain protein targets are available to bind due to similar nonradioactive POX blockade. As a result, a reduction of the net accumulation of radioactivity would be observed. This premise was examined using PET imaging in which the in vivo radioactivity distributions were measured in rats after injection of [^{11}C]POX in naïve, 20 and 60 minutes after 250 μg/kg nonradioactive POX.

Typical PET imaging sagittal views (Fig. 13, 0- to 30-minute summed radioactivity signal) show that the CNS radioactivity in naïve rats is decreased substantially after nonradioactive POX pretreatment at both the 20- and 60-minute time points due to blockade of enzymes by nonradioactive POX. However, relative to the 20-minute time point, there is an increase in the amount of brain radioactivity at 60 minutes (Fig. 13). The greater amount of radioactivity in brain at 60 minutes after unlabeled POX radioactivity is consistent with our prior supposition that CNS proteins are initially modified by nonradioactive POX at 20 minutes but that by 60 minutes a fraction of these proteins can undergo reaction with the [^{11}C]POX tracer. This possibility is supported by the finding that in naïve rats after [^{11}C]POX injection, steady radioactivity levels are found after a few minutes, which is thought to be due to covalent modification of proteins by the tracer. Therefore, the nonradioactive POX pretreatment scenario after the increase

in brain radioactivity at 60 minutes relative to 20 minutes is most likely due to an increase in available functional target proteins (e.g., reactivated) allowing [^{11}C]POX tracer to modify these targets. This observation rules out aging, since aged protein targets would remain refractory to reactivation and unable to covalently bind the [^{11}C]POX tracer.

Comparison of PET Imaging OP Tracers: CNS Radioactivity Distributions. Given the shared mechanism of enzyme inactivation by OPs and the high concentration of AChE in the CNS, imaging time-activity curves were compared in brain between [^{11}C]POX and previously reported OP-based PET imaging tracers (Fig. 14) (Neumann et al., 2017, 2018; Hayes et al., 2018, 2019, 2020, 2021). The rat brain SUV activity data for [^{11}C]POX (blue curve) is significantly higher but similar in profile to brain TACs from other OP tracers. All tracers were injected intravenously and showed an initial rapid radioactivity uptake in brain followed by a steady, elevated SUV level over 30 minutes. The level [^{11}C]POX-derived SUV profile without apparent radioactivity washout over 30 minutes is consistent with covalent modification of protein targets in the CNS (Fig. 14) that cannot undergo washout.

[^{11}C]POX also afforded higher brain SUV activity levels than the other four OP tracers evaluated in rat. All tracers contain a p-nitrophenol as leaving group, but [^{18}F]sarin analog and [^{18}F]VX analog contain a fluorine atom that can influence the tissue activity uptake profiles. Still, each OP tracer inhibits AChE covalently (Fig. 14). [^{11}C]POX affords higher brain AUC and SUV levels (Table 1) than the other OP tracers because phosphates are higher reactivity than phosphonates; the latter contain adjacent sp3 centers (P-C bond) that reduce reaction with serine esterase (Figs. 1 and 14). [^{11}C]POX itself may also achieve greater and/or faster initial penetration into brain than the phosphonates, but this seems unlikely because [^{11}C]POX is extensively metabolized in minutes (Fig. 4). Additional in vivo experiments are ongoing to further probe mechanisms involved that result in higher radioactivity levels in brain after [^{11}C]POX injection relative to the phosphonate tracers (Fig. 14).

TABLE 1
Brain AUC$_{0-15\ min}$ and SUV$_{max}$ (mean ± S.E.M.)
Tracer structures and analogs are shown in Fig. 14. Values are one-way ANOVA. $P = 0.0715$ for AUC$_{0-15\ min}$ and $P = 0.136$ for SUV$_{max}$.

Tracer	AUC$_{0-15\ min}$	SUV$_{max}$
[^{11}C]POX	23.0 ± 1.5	1.58 ± 0.1
[^{11}C]Sarin analog	18.1 ± 0.8	1.29 ± 0.06
[^{11}C]VX analog	15.0 ± 1.3	1.08 ± 0.09
[^{18}F]Sarin analog	16.2 ± 1.1	1.20 ± 0.08
[^{18}F]VX analog	19.8 ± 0.5	1.40 ± 0.04

Discussion

This work describes for the first time the synthesis and pharmacokinetics of carbon-11–labeled paraoxon [^{11}C]POX, a PET tracer of one of the most widely used compounds to study the biochemistry, in vivo biodistribution, and toxicity of reactive organophosphate compounds. Prior PET imaging OP tracer studies used [^{18}F]fluorine-labeled and/or leaving group analogs of OP chemical agents (James et al., 2014; Neumann et al., 2017, 2018; Hayes et al., 2018, 2019, 2020, 2021; Thompson et al., 2020). [^{11}C]POX is an exact isotopic replica of a reactive OP in which the in vivo data accurately reflects that of nonradioactive paraoxon. This is vitally important for interpretation of the [^{11}C]POX tracer biodistribution and arterial data in naïve rats because tracer-only doses correspond to a very low exposure of POX and the ultrasensitive PET imaging of tissue and blood could be examined. To our knowledge, this the first time that an ultralow picograms POX exposure has been analyzed in live animals. Even at this very low dose, evidence of POX rapidly entering brain and persisting in brain was found.

Tissue and arterial blood radioactivity distributions in rats given [^{11}C]POX via a subcutaneous route had lower tissue AUC values than rats given [^{11}C]POX by intravenous injection. However, the brain-to-tissue ratios for intravenous and subcutaneous routes suggested less POX distributed to the tissues via the subcutaneous route compared with intravenous dosing, but the relative radioactivity distribution across tissues were similar.

This PET tracer study was also able to quantify, locate, and acquire the time course of radiolabeled targets in a model of OP toxicity in which a nonradioactive dose of paraoxon (250 μg/kg, LD$_{50}$) was given followed by [^{11}C]POX tracer as a means to probe reactive target interactions at 20- and 60-minute time points. This experimental approach afforded insights into the dynamic mechanism of paraoxon in live animals. Using [^{11}C]POX as a probe, it was shown that unlabeled paraoxon blocked a preponderance of reactive targets at 20 minutes; however, by 60 minutes there was an increase in target availability. The change at 60 minutes may occur because the LD$_{50}$ dose of paraoxon ($\sim$14 μM; 250 ug/kg into 20 m blood) is insufficient to saturate all available paraoxon-targeted proteins but is enough to significantly reduce their availability for the radioactive probe. Assuming that the target site concentration drops by an order to two orders of magnitude after nonlabeled POX is given, the rate of covalent inhibition by radioactive paraoxon would be significantly reduced. This occurs because the rate of covalent inhibition is determined by the protein target concentration (typically high nM or low μM) and greater than the [^{11}C]POX concentration (est. $\sim$20 pM). In the absence of nonlabeled paraoxon (e.g., naïve), the covalent reaction with [^{11}C]POX will be fast ($t_{1/2} < 1$ minute) (Fig. 4) but will drastically slow down (10- to 100-fold) when most rate-determining targets are unavailable for reaction. When nonlabeled POX is given the target concentrations will drop, and the reactions need to run for $\sim$60 minutes to reach labeling levels normally observed in the absence of nonlabeled POX. This notion is consistent with expanded target accessibility in some tissues for the labeled probe once the majority of target sites were covalently occupied by the nonlabeled paraoxon.

The data showed that unlabeled paraoxon blocked the preponderance of reactive targets at 20 minutes with a return to near-naïve levels by 60 minutes. When compared with other OP PET tracers with the *p*-nitrophenoxy leaving group and where all tracers retained brain levels over the time course of the experiment consistent with covalent modification, brain radioactivity levels for [^{11}C]POX were elevated 50% higher compared with the other OP PET tracers studied previously. In sum, this study found that the novel [^{11}C]POX PET imaging tracer displays optimal properties as a representative organophosphate positron-labeled probe that can effectively serve in future in vivo, ex vivo, and in vitro studies to assess the extent of target modifications and/or the efficacy of oxime antidotes to reactivate OP-modified targets.

Data Availability

NMR or paraoxon, chromatograms of the reversed-phase HPLC profiles of the crude material semipreparative purification, and the quality control (QC) dose profiles are provided.

Authorship Contributions

Participated in research design: VanBrocklin, Zinn, Gerdes, Thompson.

Conducted experiments: Hayes, Blecha, Huynh, Zinn, Thompson.

Contributed new reagents or analytic tools: Hayes, Chao, Blecha, Thompson.

Performed data analysis: Hayes, Chao, Blecha, VanBrocklin, Gerdes, Thompson.

Wrote or contributed to the writing of the manuscript: Hayes, Chao, Blecha, VanBrocklin, Gerdes, Thompson.

References

Ametamey SM, Honer M, and Schubiger PA (2008) Molecular imaging with PET. *Chem Rev* **108**:1501–1516.

Ballantyne B and Marrs TC (1992) *Clinical and Experimental Toxicology of Organophosphates and Carbamates*, Butterworth-Heinemann Ltd, Oxford, UK.

Blomqvist G, Tavitian B, Pappata S, Crouzel C, Jobert A, Doignon I, and Di Giamberardino L (2001) Quantitative measurement of cerebral acetylcholinesterase using. *J Cereb Blood Flow Metab* **21**:114–131.

Chao CK, Ahmed SK, Gerdes JM, and Thompson CM (2016) Novel organophosphate ligand O-(2-fluoroethyl)-O-(p-nitrophenyl)methylphosphonate: synthesis, hydrolytic stability and analysis of the inhibition and reactivation of cholinesterases. *Chem Res Toxicol* **29**:1810–1817.

Davison AN (1953) Return of cholinesterase activity in the rat after inhibition by organophosphorus compounds. I. Diethyl p-nitro-phenyl phosphate (E 600, paraoxon). *Biochem J* **54**:583–590.

Dettbarn WD, Yang ZP, and Milatovic D (1999) Different role of carboxylesterases in toxicity and tolerance to paraoxon and DFP. *Chem Biol Interact* **119–120**:445–454.

Eisenkraft A, Falk A, and Finkelstein A (2013) The role of glutamate and the immune system in organophosphate-induced CNS damage. *Neurotox Res* **24**:265–279.

Erdos EG and Boggs LE (1961) Hydrolysis of paraoxon in mammalian blood. *Nature* **190**:716–717.

Everett NB, Simmons B, and Lasher EP (1956) Distribution of blood (Fe 59) and plasma (I 131) volumes of rats determined by liquid nitrogen freezing. *Circ Res* **4**:419–424.

Fagerlind L, Holmstedt B, and Wallen O (1952) Preparation and determination of diethyl p-nitrophenyl phosphate (E 600) a drug used in the treatment of glaucoma. *Sven Farm Tidskr* **56**:303–308.

Farizatto KLG and Bahr BA (2017) Paraoxon: an anticholinesterase that triggers an excitotoxic cascade of oxidative stress, adhesion responses, and synaptic compromise. *Eur Sci J* **13**:29–37.

Fletcher JH, Hamilton JC, Hechenbleikner I, Hoegberg EI, Sertl BJ, and Cassaday JT (1950) The synthesis of parathion and some closely related compounds. *J Am Chem Soc* **72**:2461–2464 DOI: 10.1021/ja01162a028.

Gambhir SS (2004) Quantitative assay development for PET, in *PET: Molecular Imaging and Its Biological Applications* (Phelps ME, ed) pp 125–216, Springer, New York.

Gearhart JM, Jepson GW, Clewell HJ, Andersen ME, and Conolly RB (1994) Physiologically based pharmacokinetic model for the inhibition of acetylcholinesterase by organophosphate esters. *Environ Health Perspect* **1994** (102 Suppl 11):51–60.

Goud NS, Bhattacharya A, Joshi RK, Nagaraj C, Bharath RD, and Kumar P (2021) Carbon-11: radiochemistry and target-based PET molecular imaging applications in oncology, cardiology, and neurology. *J Med Chem* **64**:1223–1259.

Hayes TR, Blecha JE, Chao CK, Huynh TL, VanBrocklin HF, Zinn KR, Taylor PW, Gerdes JM, and Thompson CM (2020) Positron emission tomography evaluation of oxime countermeasures in live rats using the tracer O-(2-[^{18}F]fluoroethyl)-O-(p-nitrophenyl)methylphosphonate [^{18}F]-VXS. *Ann N Y Acad Sci* **1479**:180–195.

Hayes TR, Blecha JE, Thompson CM, Gerdes JM, and VanBrocklin HF (2019) Divergent synthesis of organophosphate [^{11}C]VX- and [^{11}C]Sarin-surrogates from a common set of starting materials. *Appl Radiat Isot* **151**:182–186.

Hayes TR, Chao CK, Blecha JE, Huynh TL, Zinn KR, Thompson CM, Gerdes JM, and VanBrocklin HF (2021) Biological distribution and metabolic profiles of carbon-11 and fluorine-18 tracers of VX- and sarin-analogs in Sprague-Dawley rats. *Chem Res Toxicol* **34**:63–69.

Hayes TR, Thompson CM, Blecha JE, Gerdes JM, and VanBrocklin HF (2018) Radiosynthesis of O-(1-[^{18}F]fluoropropan-2-yl)-O-(4-nitrophenyl)methylphosphonate: a novel PET tracer surrogate of sarin. *J Labelled Comp Radiopharm* **61**:1089–1094.

Hiraoka K, Okamura N, Funaki Y, Watanuki S, Tashiro M, Kato M, Hayashi A, Hosokai Y, Yamasaki H, Fujii T, et al. (2009) Quantitative analysis of donepezil binding to acetylcholinesterase using positron emission tomography and [5-(11)C-methoxy]donepezil. *Neuroimage* **46**:616–623.

James SL, Ahmed SK, Murphy S, Braden MR, Belabassi Y, VanBrocklin HF, Thompson CM, and Gerdes JM (2014) A novel fluorine-18 β-fluoroethoxy organophosphate positron emission tomography imaging tracer targeted to central nervous system acetylcholinesterase. *ACS Chem Neurosci* **5**:519–524.

Kardos SA and Sultatos LG (2000) Interactions of the organophosphates paraoxon and methyl paraoxon with mouse brain acetylcholinesterase. *Toxicol Sci* **58**:118–126.

Kikuchi T, Okamura T, Zhang M-R, Fukushi K, and Irie T (2010) In vivo evaluation of N-[18F]fluoroethylpiperidin-4ylmethyl acetate in rats compared with MP4A as a probe for measuring cerebral acetylcholinesterase activity. *Synapse* **64**:209–215.

Koeppe RA, Frey KA, Snyder SE, Meyer P, Kilbourn MR, and Kuhl DE (1999) Kinetic modeling of N-[11C]methylpiperidin-4-yl propionate: alternatives for analysis of an irreversible positron emission tomography trace for measurement of acetylcholinesterase activity in human brain. *J Cereb Blood Flow Metab* **19**:1150–1163.

Krishnan BR, Winwood D, and Bodor N (1990) A convenient preparation of phosphate diester monoanions. *Synth Commun* **20**:2653–2658 DOI: 10.1080/00397919008051473.

Krishnan JKS, Figueiredo TH, Moffett JR, Arun P, Appu AP, Puthillathu N, Braga MF, Flagg T, and Namboodiri AM (2017) Brief isoflurane administration as a post-exposure treatment for organophosphate poisoning. *Neurotoxicology* **63**:84–89.

Lichtenstein EP, Fuhremann TW, Hochberg AA, Zahlten RN, and Stratman FW (1973) Metabolism of (14 C)parathion and (14 C)paraoxon with fractions and subfractions of rat liver cells. *J Agric Food Chem* **21**:416–424.

Loening AM and Gambhir SS (2003) AMIDE: a free software tool for multimodality medical image analysis. *Mol Imaging* **2**:131–137.

Mastin TW, Norman GR, and Weilmuenster EA (1945) Chemistry of the aliphatic esters of thiophosphoric acids. I. *J Am Chem Soc* **67**:1662–1664 DOI: 10.1021/ja01226a014.

Maxwell DM (1992) The specificity of carboxylesterase protection against the toxicity of organophosphorus compounds. *Toxicol Appl Pharmacol* **114**:306–312.

Morita H (1995) Neurotoxicity of nerve agents. *No To Shinkei* **47**:1129–1134.

Nakatsugawa T, Tolman NM, and Dahm PA (1969) Degradation of parathion in the rat. *Biochem Pharmacol* **18**:1103–1114.

Neal RA (1967) Studies on the metabolism of diethyl 4-nitrophenyl phosphorothionate (parathion) in vitro. *Biochem J* **103**:183–191.

Neumann KD, Blecha JE, Hayes TR, Huynh T, Chao C-K, Guilloteau N, Zinn KR, VanBrocklin HF, Thompson CM, and Gerdes JM (2018) Radiosynthesis, ex vivo biodistribution, and in vivo positron emission tomography imaging evaluations of [^{11}C]2-pyridinealdoxime methiodide ([^{11}C]2-PAM): a first-in-class antidote tracer for organophosphate intoxication. *ACS Chem Neurosci* **9**:3007–3014.

Neumann KD, Thompson CM, Blecha JE, Gerdes JM, and VanBrocklin HF (2017) An improved radiosynthesis of O-(2-[^{18}F]fluoroethyl)-O-(p-nitrophenyl)methylphosphonate: a first-in-class cholinesterase PET tracer. *J Labelled Comp Radiopharm* **60**:337–342.

Pappata S, Tavitian B, Traykov L, Jobert A, Dalger A, Mangin JF, Crouzel C, and DiGiamberardino L (1996) In vivo imaging of human cerebral acetylcholinesterase. *J Neurochem* **67**:876–879.

Paxinos G (2015) Preface, in *The Rat Nervous System*, 4th ed (Paxinos G, ed) p xi, Academic Press, Cambridge, MA.

Paxinos G and Watson C (2007) *The Rat Brain in Stereotaxic Coordinates*, 6th ed, Academic Press, Cambridge, MA.

Planas AM, Crouzel C, Hinnen F, Jobert A, Né F, DiGiamberardino L, and Tavitian B (1994) Rat brain acetylcholinesterase visualized with [11C]physostigmine. *Neuroimage* **1**:173–180.

Rojas A, Ganesh T, Wang W, Wang J, and Dingledine R (2020) A rat model of organophosphate-induced status epilepticus and the beneficial effects of EP2 receptor inhibition. *Neurobiol Dis* **133**:104399.

Shinotoh H, Fukushi K, Nagatsuka S, and Irie T (2004) Acetylcholinesterase imaging: its use in therapy evaluation and drug design. *Curr Pharm Des* **10**:1505–1517.

Song X, Pope C, Murthy R, Shaikh J, Lal B, and Bressler JP (2004) Interactive effects of paraoxon and pyridostigmine on blood-brain barrier integrity and cholinergic toxicity. *Toxicol Sci* **78**:241–247.

Taylor P (2018) Anticholinesterase Agents, in *Goodman & Gilman's: The Pharmacological Basis of Therapeutics*, 13th ed (Brunton LL, Hilal-Dandan R, and Knollmann BC, eds) pp 163–176, McGraw-Hill Education, New York.

Thompson CM, Gerdes JM, and VanBrocklin HF (2020) Positron emission tomography studies of organophosphate chemical threats and oxime countermeasures. *Neurobiol Dis* **133**:104455.

Timchalk C, Nolan RJ, Mendrala AL, Dittenber DA, Brzak KA, and Mattsson JL (2002) A Physiologically based pharmacokinetic and pharmacodynamic (PBPK/PD) model for the organophosphate insecticide chlorpyrifos in rats and humans. *Toxicol Sci* **66**:34–53.

Turner PV, Brabb T, Pekow C, and Vasbinder MA (2011) Administration of substances to laboratory animals: routes of administration and factors to consider. *J Am Assoc Lab Anim Sci* **50**:600–613.

Volkow ND, Ding YS, Fowler JS, and Gatley SJ (2001) Imaging brain cholinergic activity with positron emission tomography: its role in the evaluation of cholinergic treatments in Alzheimer's dementia. *Biol Psychiatry* **49**:211–220.

Volpe MT, Bisso GM, and Michalek H (1990) In vivo and in vitro effects of diisopropyl fluorophosphate on individual molecular forms of rat brain acetylcholinesterase. *Neurochem Res* **15**:975–979.

Voorhees JR, Remy MT, Erickson CM, Dutca LM, Brat DJ, and Pieper AA (2019) Occupational-like organophosphate exposure disrupts microglia and accelerates deficits in a rat model of Alzheimer's disease. *NPJ Aging Mech Dis* **5**:3.

Voorhees JR, Rohlman DS, Lein PJ, and Pieper AA (2017) Neurotoxicity in preclinical models of occupational exposure to organophosphorus compounds. *Front Neurosci* **10**:590.

Walker WF and Homberger DG (1997) *Anatomy and Dissection of the Rat*, 3rd ed, W. H. Freeman and Company, New York.

Worek F, Aurbek N, Wille T, Eyer P, and Thiermann H (2011) Kinetic analysis of interactions of paraoxon and oximes with human, rhesus monkey, swine, rabbit, rat and guinea pig acetylcholinesterase. *Toxicol Lett* **200**:19–23.

Zare Z, Tehrani M, Zarbakhsh S, Farzadmanesh H, Shafia S, Abedinzade M, Ghanaat A, and Mohammadi M (2020) Effects of paraoxon exposure on expression of apoptosis-related genes, neuronal survival, and astrocyte activation in rat prefrontal cortex. *Neurotox Res* **37**:356–365.

Address correspondence to: Charles M. Thompson, Department of Biomedical and Pharmaceutical Sciences, University of Montana, 32 Campus Drive, Missoula, MT 59812. E-mail: cthompson@hbri.org